

Energy-level statistics in planar fractal tight-binding models

Qi Yao ^{1,2} Xiaotian Yang ^{1,2} Askar A. Iliasov,² M. I. Katsnelson ² and Shengjun Yuan ^{1,3,*}

¹Key Laboratory of Artificial Micro- and Nano-structures of Ministry of Education and School of Physics and Technology, Wuhan University, Wuhan, Hubei 430072, China

²Institute for Molecules and Materials, Radboud University, Heijendaalseweg 135, 6525 AJ Nijmegen, The Netherlands

³Wuhan Institute of Quantum Technology, Wuhan 430206, China

 (Received 1 October 2022; revised 14 February 2023; accepted 9 March 2023; published 24 March 2023)

In this study, we examine the statistics of level spectra in a noninteracting electron gas confined to a *Sierpiński carpet* lattice. These lattices are constructed using two types of the *self* and *gene* patterns, and they are categorized by the area-perimeter scaling law. The singularly continuous spectra, along with the nearest level spacing distribution and gap-ratio distribution, reveal a critical phase different from both extended and localized phases. This critical phase differs from the behavior near the Anderson model's metal-insulator transition. The Wigner-like conjecture is confirmed for both lattice classes, indicating Gaussian orthogonal symmetry. A similar observation was made in a quasiperiodic lattice [*Phys. Rev. Lett.* **80**, 3996 (1998)]. The self-similar nature of fractals also leads to level clustering behavior.

DOI: [10.1103/PhysRevB.107.115424](https://doi.org/10.1103/PhysRevB.107.115424)

I. INTRODUCTION

Fractals have two perspectives. The first is the irregular geometry found in natural objects such as clouds and mountains [1–5]. These shapes are invariant, either deterministically or statistically, on any scale size. Examples include a Cantor set [1], a *Sierpiński* lattice [3,6], a Vicsek lattice [7,8], a Koch curve [9], boundary modes of lattices [10–13], and random regular graphs [14]. The second perspective is the self-similarity behaviors of quantum counterparts, seen in the Hofstadter butterfly spectra [15] and in the level distribution, density of states (DOS), and wave function of electronic properties [16–18].

Some researchers advocate that fractals and quasicrystals are *intermediate structures* between crystalline and amorphous systems [19–21]. Both lose translation symmetry but maintain the long-range order. Theoretically, the one-dimensional (1D) Fibonacci chain and the 2D Penrose tiling [22,23] are suggested for quasicrystals lattices. The first observation of a quasicrystalline Al-Mn alloy was made through its diffraction patterns [24], which implies multifold rotational symmetry [25].

Recently, fractals have been attracting growing interest due to engineered fractals in experiments [26–32] and several crucial works [33,34]. Researchers are interested in (i) further classifying fractals using various topology characters, such as topological dimension [1], the order of ramification [33,35], connectivity [1,36], lacunarity [37–41], etc.; (ii) studying material properties, such as quantum transport [42,43], Hall conductivity [44], optical spectra [45], and plasmon mode [46]; (iii) exploring other systems such as spin [33,47], photon [48], and harmonic oscillators [12,49] on these lattices. In this

work, we focus on the *Sierpiński carpet* [1,5,33,47], which belongs to a larger family of fractal constructions and has an infinite order of ramification. It resembles a translation-invariant square lattice in 2D and can be fabricated using medium-scale optical waveguide arrays [50,51] or photonic lattices [43] ($g \in [3, 5]$, where g is defined in the context below) or more extreme methods such as local-field tailoring [52].

Sierpiński carpet. Let us denote a *Sierpiński carpet* lattice as $SC(n, m, g)$, which can be experimentally realized using approaches similar to those described in previous works [43,50,51]. The hierarchy level g is a measure of scale invariance [1,3], which becomes apparent when scaling these structures. To construct the lattice, we need two ingredients: the generator(n, m) and the dilation pattern. The generator(n, m) serves as a “seed” lattice, which is constructed as follows: a square lattice of size n by n is created, and then a subsquare lattice of size m by m is removed from its center [53]. It is assumed that the generator(n, m) is symmetrical, hence n is always larger than m , and $n - m$ is an even number. n (m) only starts from 3 (1), followed by 4 (2), 5 (1, 3), 6 (2, 4), and so on (refer to Table I). The dilation pattern involves selecting two representatives, M_{se} and M_{ge} , with matrix form as the *self* and *gene* patterns, respectively.

Using the generator(n, m) and the two patterns, we can dilate two classes of the $SC(n, m, g)$ lattice using the following equation [Eq. (1)]:

$$SC(n, m, g) = M_{se,ge}(g) \otimes \text{generator}(n, m). \quad (1)$$

g is reduced with $M_{se,ge}(g) \equiv M_{se,ge}(g-1) \otimes M_{se,ge}(1)$, and the symbol \otimes represents the tensor product of the matrices. There are two important points to note about $M_{se,ge}$: (i) The matrix M_{se} has r^2 elements, consisting of \mathcal{N} ones and $r^2 - \mathcal{N}$ zeros. The perimeter length of the $SC(n, m, g)$ lattice increases by r times and its area increases by \mathcal{N} times when g increases

*Corresponding author: s.yuan@whu.edu.cn

TABLE I. Planar SC(n, m, g^*) lattices with peculiar configurations between the generator(n, m) and the *self* or *gene* patterns are classified into two subclasses based on the area-perimeter scaling law [5,54]. The Hausdorff dimensions (\mathcal{D}_{se} and \mathcal{D}_{ge}) are listed in lines 2 and 5, respectively. The maximum energy (E_m) is taken from Figs. 2(a1), 2(b1), 2(c1), and 2(d1), and the mean gap-ratio ($\langle \bar{r} \rangle$) is calculated from the \bar{r} -value statistic in Fig. 4. The values of E_m and $\langle \bar{r} \rangle$ are listed in the parentheses (...), which are sequentially increased with increasing g^* value [63] from 2. For example, the values (3.2369, 3.3035, 3.3065) in the illustration cell (3.2693, 3.3035, 3.3065) indicate that E_m is 3.2369, 3.3035, and 3.3065 in units of t for the SC(5, 3, 2), SC(5, 3, 3), and SC(5, 3, 4) lattices, respectively.

SC(n, m, g^*)		(5, 3)	(4, 2)	(3, 1)	(5, 1)
		1.8928	1.8928	1.8928	1.8928
self	E_m	(3.2693, 3.3035, 3.3065)	(3.2940, 3.3492, 3.4563)	(2.9498, 3.3519, 3.4455, 3.4563)	(3.7857, 3.8263)
	$\langle \bar{r} \rangle$	(0.1437, 0.1353, 0.1433)	(0.1492, 0.1585, 0.1496)	(0.1951, 0.1503, 0.1556, 0.1605)	(0.1830, 0.1912)
		1.7227	1.7925	1.8928	1.9746
gene	E_m	(2.9479, 3.2818)	(2.9250, 3.3050, 3.3484)	(2.9498, 3.3519, 3.4455, 3.4563)	(3.8106, 3.8647)
	$\langle \bar{r} \rangle$	(0.1158, 0.0980)	(0.1419, 0.1231, 0.1150)	(0.1951, 0.1503, 0.1556, 0.1605)	(0.1773, 0.1984)

Note: we compute $\mathcal{D}_{\text{se}} = 1.8928$ with $\mathcal{N} = 8$ and $r = 3$.

by 1. The elements in M_{se} can be placed flexibly, which might result in several subclusters in the spatial lattice and energy spectra (see the *vari* pattern, a variation of the *self* pattern, in Appendix A). The *self* pattern and its accessible geometry dimension, \mathcal{D}_{se} , have been studied extensively [11,42]. (ii) M_{ge} is exactly determined by the graphical mapping of an individual generator(n, m). Its size is n by n , and all elements consist of $n^2 - m^2$ ones and m^2 zeros. To visualize the two pattern classes, consider the case with the generator(4, 2) in Fig. 1. Setting $r = 3$ and $\mathcal{N} = 8$ yields $M_{\text{se}} = [1, 1, 1; 1, 0, 1; 1, 1, 1]$ and $M_{\text{ge}}(1) = [1, 1, 1, 1; 1, 0, 0, 1; 1, 0, 0, 1; 1, 1, 1, 1]$. Equation (1) can be iterated infinitely to obtain SC(n, m, ∞) or finitely for prefractal SC(n, m, g). These lattices can be classified into two scale-invariant classes.

The area-perimeter scaling law [5,54] $Ar \propto p^{\mathcal{D}}$ discriminates these two SC(n, m, g) classes by dimension index \mathcal{D} . Physically, this quantity defines the filling factor of the SC(n, m, g) lattice in 2D space, sometimes called *Hausdorff dimension* \mathcal{D}_H . It is known that, by enumerating the vertex number in these two classes, the perimeter length is $p = mr^g$ and the area is $Ar = (n^2 - m^2)\mathcal{N}^g$ for the *self* pattern, and $p = m^{g+1}$ and $Ar = (n^2 - m^2)^{g+1}$ for the *gene* pattern. We note that the exponential factor of p and Ar is g and $g + 1$, respectively. This signifies that the geometrical hierarchy is scaled extraordinarily once in the *gene* pattern (see Fig. 1).

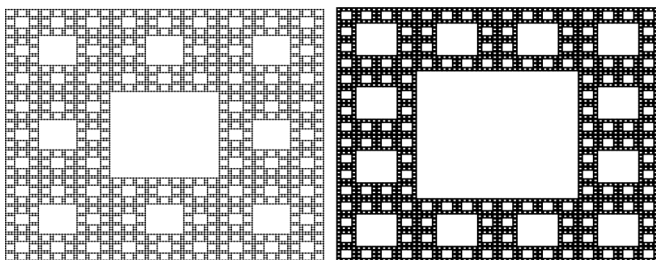


FIG. 1. Pictorial sketch of prefractals in the SC(n, m, g) family by the paradigmatic generator(4, 2) under the *self* and *gene* patterns. The corresponding spatial atom clusters are shown in the left and right panels, respectively, at a hierarchical level of $g = 3$. The dilation of the *self* pattern is easily captured by $\mathcal{D}_{\text{se}} = \ln(\mathcal{N})/\ln(r)$, where we set $\mathcal{N} = 8$ and $r = 3$ for simplification when g increases by 1. Conversely, the *generator* predetermines M_{ge} (see the main text for its definition). More cases can be found in Table I.

Scaling two SC(4, 2, 3) lattices to the same size, the lattice in the *gene* pattern has a darker black color than that in the *self* pattern.

To address this incorrect definition, we introduce the concept of the geometric hierarchy level g^* . Through some algebraic calculations, in the limit of large g , we obtain two asymptotic formulas: $\mathcal{D}_{\text{se}} = \ln(\mathcal{N})/\ln(r)$ and $\mathcal{D}_{\text{ge}} = \ln(n^2 - m^2)/\ln(n)$. Notably, \mathcal{D}_{ge} only depends on its *generator*(n, m), while \mathcal{D}_{se} is related to the choice of external self-similarity. \mathcal{D} affects the transport properties. Van Veen *et al.* reported the box-counting dimension \mathcal{D}_{box} from numerical simulations of quantum conductance fluctuations, which is consistent with \mathcal{D}_{se} [42]. In a *Sierpiński* lattice sample of CO molecules on a Cu (111) surface [31], Kempkes *et al.* experimentally derived the dimension \mathcal{D}_ψ from the electronic wave function ψ .

Upon these SC(n, m, g^*) lattices, a noninteracting electron gas is considered. We model it by

$$H = - \sum_{\langle i, j \rangle} (\mathbf{c}_i^\dagger \mathbf{c}_j + \mathbf{c}_j^\dagger \mathbf{c}_i) + \sum_i V \mathbf{c}_i^\dagger \mathbf{c}_i. \quad (2)$$

A single Wannier orbital $\mathbf{c}_i^\dagger |0\rangle$ is at site index i , and the symbol $\langle i, j \rangle$ labels the nearest-neighbor site pair. We set $V = 0$, hence there is only the kinetic term (in other words, the properties of this model result purely from the fractal geometry, which typically consists of broken translation symmetry and the long-range order of scaling symmetry about g^*). We diagonalize the model and obtain its energy spectra and eigenwave functions.

We introduce two essential tools to extract information from the energy spectra. The first is the local band-branching predictions, which is discussed in Sec. II B. We now discuss the other tool, the level-spacing distribution (LSD) between the adjacent energy levels. As a prelude to this work, Iliasov *et al.* [55,56] studied the LSD in two simplified iterated structures (each square- and triangle-block unit with fewer connections [56], respectively). They exploited the decimating procedure, and gave the analytical asymptotic formula $P(s) \sim s^\alpha$ at the decay tail, where s is the nearest-neighbor level spacing, α is a constant, and $P(s)$ is the distribution.

Two points are worth noting: (i) The unexpected peak at the tail of the numerical $P(s)$ observed in [55] is due to the absence of an unfolding procedure. (ii) Although the model is nonrandom on these two lattices, it belongs to the Gaussian

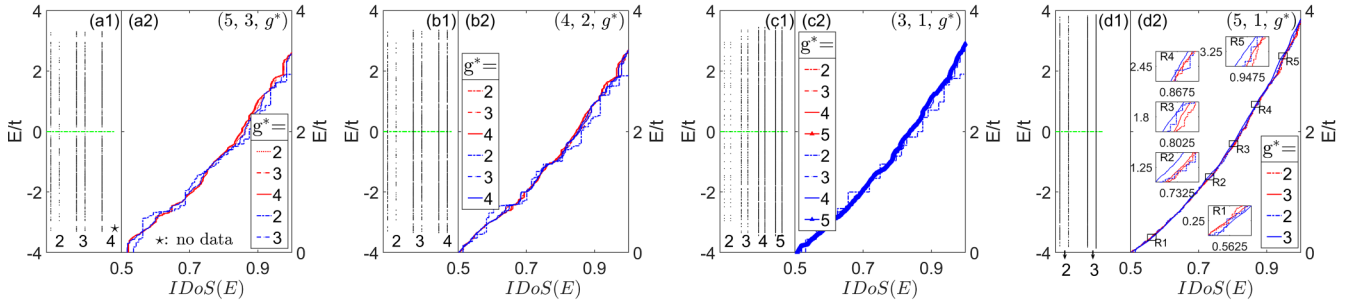


FIG. 2. The allowed energy spectra and the half-branch integrated density of states (IDOS) change with the configuration of a generator(n, m) and geometrical hierarchy level g^* . In (a1), full band structures are plotted in pairs for the *self* and *gene* patterns, which are related to the red and blue color IDOS(E) in (a2) for the generator(5, 3), respectively. Similarly, the other three generator cases of (4,2), (3,1), and (5,1) in Table I are shown for the band structures in (b1), (c1), and (d1); and for the IDOS(E) in (b2), (c2), and (d2). Each IDOS(E) is calculated using the histogram $\rho(E) = 1/A \sum_m \delta(E - E_m)$ and its integrated region ranges from -4 to 4 . As g^* increases to its maximum value [63], the green dotted line $E = 0$ is added to display the level-distribution symmetry. In (d2), five insets (R1 – R5) zoom in on the IDOS(E) at different positions.

orthogonal ensemble [57–59] and may obey the Wigner-like surmise. By making a Taylor series expansion of the tail of $P(s)$, a power-law scaling is found in the large spacing region, and the value of α depends on the size of the lattice. This result is supported even in these $SC(n, m, g^*)$ fractals. Zhang *et al.* [60] were the first to pioneer this possibility in quasicrystals. According to random matrix theory (RMT) [61], there are three kinds of LSDs: the Poisson (Wigner) distributions for the localized (extended) phases, and an intermediate distribution for the critical phase.

In this work, we explore the energy spectra and the LSDs about the $SC(n, m, g^*)$ lattices. We find that a critical phase (CP) exists in our model, with all states being critical, and affected by disorder [62]. Additionally, we observe level clustering, which can be considered a special case of level attraction.

The paper is structured as follows: In Sec. II A, we review the band structure of the $SC(n, m, g^*)$ lattices. Section II B analyzes the energy distribution, and Sec. II C studies the energy correlations using the nearest level spacing distribution and gap-ratio distribution. In Sec. II D, we fit the data to the Wigner-like surmise. In the conclusion (Sec. III), we compare the results with other fractals and quasicrystals and present the final conclusions. Appendixes A and B provide additional information on the level density and numerical unfolding procedure, respectively.

II. ENERGY LEVEL STATISTICS ANALYSIS

In Sec. II A, we first discuss the general characteristics of the level density, and then we explain how it is influenced by various factors, including the generator(n, m), two dilation patterns (M_{se} and M_{ge}), and the g^* value. In Sec. II B, we use the local energy cluster and integrated DOS to diagnose the whole energy spectra as singularly continuous, suggesting a critical phase. In Sec. II C, we extract the level correlation information from the approximate levels using $P(s)$ and $P(\bar{r})$. The differences in their numerical characteristics from the extended and localized phases manifest that the electronic states are in a critical phase, and $P(s)$ also indicates that they are near the Anderson transition. Finally, in Sec. II D, fittings of $P_{fit}(s)$

at various s regions with lattice size Ar of approximately 10^4 or larger confirm the Wigner-like conjecture.

A. Level density and its bandwidth

For a single electron in a $SC(n, m, g^*)$ lattice, the energy spectra for Eq. (2) with zero on-site potentials are symmetric about 0 due to the bipartite lattice. We set the hopping strength t as the energy unit, so $t = 1$. The local sites have a coordination number of 2, 3, or 4, so the energy range for all $SC(n, m, g^*)$ lattices is fixed from $-4t$ to $4t$.

Figures 2(a1), 2(b1), 2(c1), and 2(d1) show these two properties, which are independent of the generator(n, m) and the iterated patterns (M_{se} and M_{ge}). At such a restricted energy range, the generator(n, m) affects the level density by the local spatial configurations of the “seed” lattice (as seen in four panels of Fig. 2). The pattern remodulates the level density through the connections between local “seed” lattices at various g^* values. Figure 7 shows the role of three patterns with $g^* = 2$ in the level legs and DOS. The huge degenerate or quasidegenerate subclusters in the left panels of Fig. 2 (as described in [64,65]) demonstrate the tendency towards level-attracting behavior, which is rooted in the fractal lattice and intensified by increasing geometrical hierarchy level g^* , as indicated by the trend of scattered points.

Furthermore, we analyze the bandwidth behavior of these planar $SC(n, m, g^*)$ lattice-based TB models using four generator(n, m) of (5,3), (4,2), (3,1), and (5,1), as shown in Table I. In Figs. 2(a1), 2(b1), 2(c1), and 2(d1), we plot the forbidden and allowed energy regions as a function of g^* and two patterns (M_{se} and M_{ge}). The level legs are transformed into scattered points for better visibility, as shown in Fig. 7. With increasing g^* , the allowed energy regions broaden in any pattern until they approach the upper limit of $4t$.

The upper bound energy E_m or the bandwidth $2E_m$ are derived from Fig. 2 and are listed in Table I. The pattern impact can be seen by fixing the value of g^* for each generator(n, m) and changing the pattern. The results show that the *self* pattern lengthens the bandwidth more effectively when g^* increases from 2 to 5, except in cases in which the two patterns intersect coincidentally, such as in the generator(3, 1) case, as

shown in Fig. 2(c1). Given that all four generators in Table I have $n^2 - m^2 \geq \mathcal{N}$ (where $\mathcal{N} = 8$), when g^* increases by one unit, the vertex network under the *gene* pattern proliferates more quickly than the *self* pattern. Thus, we conclude that the choice of pattern affects the bandwidth, with the *self* pattern being more advantageous.

Interestingly, in Fig. 2(d1) for the generator(5, 1) case, the bandwidth approaches the upper energy limit of $4t$ after g^* reaches 2 or 3. Moreover, far from the band center, there is little change other than the intensification of the degenerate behavior when $g^* \geq 3$, and this can be generalized to the case of infinite g^* .

B. The band-branching trait and its tendency

In Sec. II B, we discuss the Anderson transition in a Fibonacci chain [66] to take advantage of the bandwidths and local band properties. Machida and Fujita scaled the raw bands into the absolute unit interval and observed a dynamic band-branching tendency with increasing disorder strength, which is strongly correlated with the overlap between wave functions and the correlation between neighboring levels. This leads us to ask whether a similar phase transition can be controlled by adjusting some lattice topological parameters [1,33,35–37].

Despite the restriction on the lattice size Ar that we can simulate, our results still provide insight into the trend of bandwidth changes and local band characteristics. At $g^* = 2$, the upper bandwidth E_m is close to or exceeds $3t$, as seen in Table I. The upper limit of E_m is $4t$, allowing for a relative extension of the rest of the bandwidth by about 25%. This can be achieved by varying generator(n, m) and/or increasing the value of g^* . Additionally, as seen in Figs. 2(a2), 2(b2), 2(c2), and 2(d2), the local band clusters show no noticeable differences in their tendencies as g^* increases.

Therefore, we conclude that under the M_{se} and M_{ge} patterns, varying generator(n, m) and g^* cannot cause a phase transition unless a $SC(n, m, g^*)$ fractal under the *gene* pattern approximates a square periodic lattice.

To further study the possible phase in the systems we consider, we examine the predictions of local band-branching theory [67–72]. A localized phase is characterized by dense-point spectra, while an extended phase has absolutely continuous spectra. A phase that lies in between is characterized by singularly continuous spectra and critical wave functions. We can obtain information about the energy gaps by integrating the DOS, $IDOS(E) = \int_{-\infty}^E \rho(E) dE$, whose vertical staircase behavior indicates the presence of energy gaps. We only consider the $E \geq 0$ branch, where the energy window is very narrow (around 0.001). By combining the above criteria and the $IDOS(E)$, we see in Fig. 2 that the energy consecutiveness property is singular and the staircase-like behavior is evident in $IDOS(E)$ for all $SC(n, m, g^*)$ lattices in Table I, except for the $SC(5, 1, 3)$ lattice under the *gene* pattern.

We are now striving to understand why the electron stays in the critical state (CS) on these fractal lattices, where the local vertex configuration appears to be more regular than in quasicrystals. Let us first explain why the other two types of states (extended and localized) cannot persist stably in

the $SC(n, m, g^*)$. Although these $SC(n, m, g^*)$ lattices have a long-range order of scaling symmetry, the Bloch (extended) waves cannot be scattered over long distances due to the absence of translation symmetry. Can a localized state exist in the fractal?

It occurs either due to Anderson localization [68] or the local design of the vertex surrounding [73–75], or both, and all or some states are in a localized phase. However, this assumption fails in the $SC(n, m, g^*)$ lattices with a pure hopping model, as there is no disorder and no unique site network for the single electron cage. Therefore, it is reasonable for a mass state cluster to be in a critical phase, and for these states to exhibit some features of extended states [65,76]. Two known cases have the CS. One is near the disorder-induced mobility edge, where the correlation length is typically comparable to the lattice size. The other is in purely frustrated lattices, where disrupted structural symmetry occurs. The $SC(n, m, g^*)$ lattices belong to the second case.

In Fig. 2(d2), the $SC(5, 1, 3)$ lattice is an exception, where the vertical staircase traits disappear obviously when $g^* = 3$ (see the five insets R1–R5). One might assume that their wave functions are extended. In the fractal reality, for a generator(n, m) with large n and small m , the proliferating lattices under the *gene* pattern can be described as a translation-symmetry lattice with some pointlike or clusterlike defects. Hence, it is reasonable that there are possible densely continuous energy spectra when g^* is significant. However, the *self* pattern precludes this possibility, as the M_{se} pattern always remains independent of the generator(n, m), even when the scaling symmetry becomes apparent by increasing the g^* value. We next study the spectral correlation in the RMT framework [77–79].

C. Level correlation statistics in two SC classes

For an energy-level set E_i , $1 \leq i \leq Ar$, where i is an integer and Ar is the area value of the dimension of the Hamiltonian H , the DOS $\rho(E)$ is divided into the smooth part $\rho_{gl}(E)$ and the local fluctuation part $\rho_{fl}(E)$. The smooth part $\rho_{gl}(E)$ must be extracted using analytical and numerical techniques; however, this is not an easy task, especially when the asymptotic form [78,80] is either difficult to obtain or leads to misleading results [81]. We define a map $\varepsilon_i = \eta(E_i)$ at the raw energy position E_i , which is obtained by interpolating the histogram $IDOS(E)$ with a cubic spline [82] (further details are available in Appendix B).

In contrast to the level-spacing distribution $P(s)$ with $s_i = \varepsilon_{i+1} - \varepsilon_i$, Oganesyan and Huse defined the gap-ratio $\tilde{r} = \min(\delta, 1/\delta)$ with $\delta = s_{i+1}/s_i$ and $s_i = E_{i+1} - E_i$ [83]. The distribution $P(\tilde{r})$ has two advantages [84,85]: (i) it does not require the estimation of $\rho_{gl}(E)$ and thus bypasses the numerical unfolding procedures, and (ii) its average value $\langle \tilde{r} \rangle$ provides information about the phase of the system. Here, we use the computed $\langle \tilde{r} \rangle$ and the statistics of $P(s)$ and $P(\tilde{r})$ to diagnose the energy spectra of the $SC(n, m, g^*)$ fractals and to quantify their phase.

In contrast to Ref. [60], degenerate levels are not removed in Figs. 3 and 4. This clearly shows how the choice of a particular generator(n, m) or an increase in g^* affects the distribution of the neighborhood bands. To determine if all states

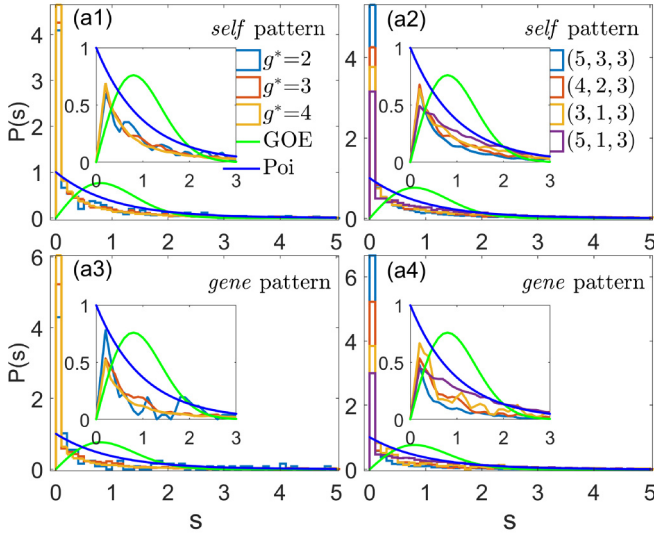


FIG. 3. The level-spacing probability distribution histogram, $P(s)$, is shown after ‘unfolding’ the raw level sequences as a function of the geometrical hierarchy level g^* or a generator (n, m) . In panels (a1) and (a3), we consider three distinct cases with $g^* = 2, 3, 4$ and $(n, m) = (4, 2)$ under the *self* and *gene* pattern, respectively. In panels (a2) and (a4), we consider four different generators of $(5, 3)$, $(3, 1)$, $(4, 2)$, and $(5, 1)$ from Table I with a fixed $g^* = 3$ under the *self* and *gene* pattern, respectively. The bin width is set to 0.1. The Poisson (solid blue line) and Wigner-surmise (solid green line) curves from Eqs. 3 are included for reference. The numerical derivation, $P(s) = -dI(s)/ds$, is shown as four insets.

are in a critical phase, we first examine the overall properties of $P(s)$. s is normalized by the mean level spacing $\langle s \rangle$ and is set in a sufficient range from 0 to 5. The unique continuity of the energy spectra has resulted in a noticeable peak in the histogram of $P(s)$ around $s = 0$ in our numerical simulations,

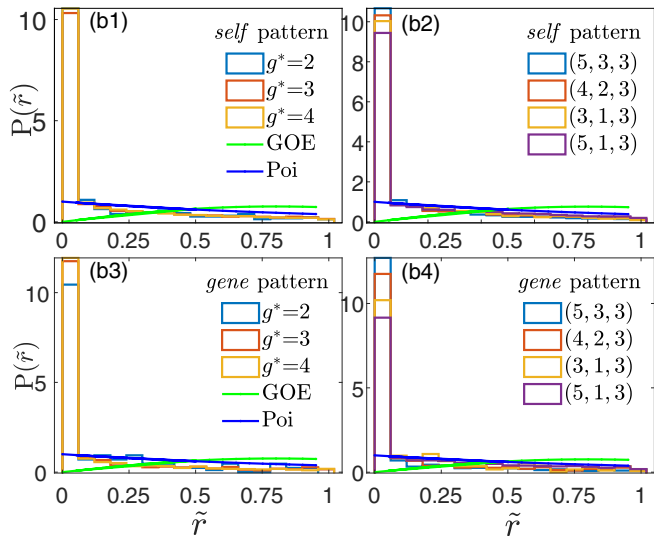


FIG. 4. The gap-ratio probability distribution histogram $P(\tilde{r})$ represents the raw levels, as shown in Fig. 3. The bin width is 0.06, and the Poisson (solid blue line) and Wigner-surmise (solid green line) curves of Eqs. (4) are included for comparison.

regardless of the dilation pattern or the configuration of the generator (n, m) and g^* . Additionally, according to RMT, $P(s)$ is neither a Poisson function for the localized phase nor a Wigner distribution for the extended phase [78], as described in Eqs. (3),

$$P_{\text{Poi}}(s) = \exp(-s),$$

$$P_{\text{GOE}}(s) = (\pi/2)s \exp(-\pi s^2/4). \quad (3)$$

Conversely, $P(s)$ has the form $c_1 s^\beta$ for small s , and it degrades into the stretched exponential form $\exp(-c_2 s^\alpha)$ in the large s range. This is a typical Wigner-like function and can be fitted in Sec. IID. By normalizing $P(s)$ and using the mean value of s , it is possible to determine the coefficients (c_1, c_2) . The indexes (β, α) can be numerically fitted, as discussed in the work of Brody, Izrailev, and Aronov *et al.* [86–89].

Similarly, using the gap-ratio \tilde{r} as a metric, Eqs. (3) have equivalent expressions [90,91],

$$P_{\text{Poi}}(\tilde{r}) = \frac{2}{(1 + \tilde{r})^2},$$

$$P_{\text{GOE}}(\tilde{r}) = \frac{27}{4} \frac{\tilde{r} + \tilde{r}^2}{(1 + \tilde{r} + \tilde{r}^2)^{5/2}}. \quad (4)$$

The mean value for the localized (extended) phase is $\langle \tilde{r} \rangle_{\text{Poi}} = 0.386$ ($\langle \tilde{r} \rangle_{\text{GOE}} = 0.536$). As seen in Table I, these levels become severely (quasi)degenerate when taking an arbitrary g^* , which causes a drop in $\langle \tilde{r} \rangle$ below 0.386. To clarify the relationship between the local band gathering and the pattern or the generator (n, m) , we employ the same approach by fixing the g^* value and comparing four generator (n, m) in D_H ascending order (see Table I). The same sequences of the generator (n, m) are also applied to the *self* pattern.

First, focusing on the *self* dilation pattern, we select the generator $(4, 2)$ case, as shown in Fig. 3(a1). The improved level clustering effect $P(s)$ rises with g^* at s close to 0, and reaches its highest height at that point, while they are often below $P_{\text{Poi}}(s)$ (blue curve in Fig. 3) until s approaches the crossover point of 2.0019 where Eqs. (3) intersect. Two crossing points, 1.2732 and 2.0019, were obtained by interpolating Eqs. (3) quantitatively. These LSDs outperform the Wigner function of $P_{\text{GOE}}(s)$ (blue curve in Fig. 3) as s steadily increases beyond it. The discrepancies between these LSDs decrease as s moves away from 0.

When $g^* = 3$, the impact of the generator (n, m) on $P(s)$ is investigated, with values taken from Table I. At small values of s , the peak height of $P(s)$ decreases for the sequences of $(5, 3)$, $(3, 1)$, $(4, 2)$, and $(5, 1)$. It is known that regardless of the generator (n, m) , D_{se} is always the same when g^* is very large. This might be explained by prefractal $\text{SC}(n, m, g^* \ll \infty)$. The alternate spectra $P(\tilde{r})$, shown in Figs. 4(b1) and 4(b2), can verify these arguments, with the histogram trends consistent with the curves in Figs. 3(a1) and 3(a2), respectively.

Now we turn to the *gene* pattern. Intuitively, the critical phase, as determined by histograms, is still distinct from the two phases defined by Eqs. (3), as seen in $P(s)$ in Figs. 3(a3) and 3(a4), and $P(\tilde{r})$ in Figs. 4(b3) and 4(b4). Additionally, two hallmarks about the peak height of $P(s)$ in the small s region can be observed: (i) The level clustering behavior of the two patterns we studied, shown in Figs. 3(a1) and 3(a3), increases as g^* increases. The peak height in the

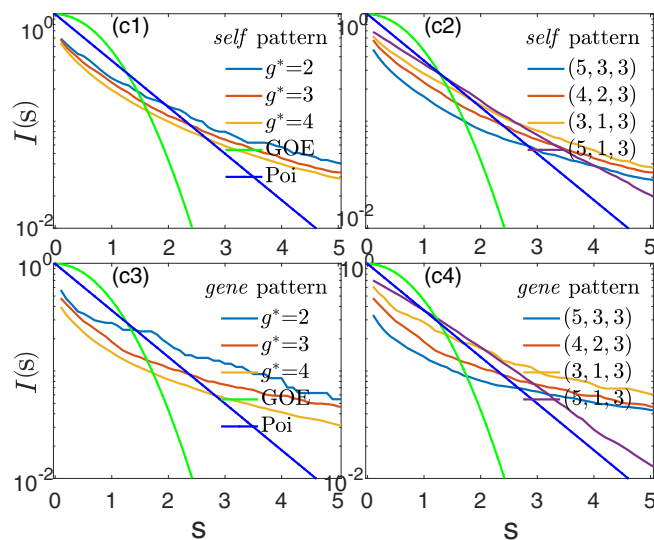


FIG. 5. The integrated level-spacing distribution, denoted as $I(s)$, has a numerical advantage over the distributions $P(s)$ and $P(\tilde{r})$. The linear-log scale displays the diverse behavior of $I(s)$ near $s = 0$ between the different cases considered. The bin width used is 0.001. The Poisson distribution (solid blue line) and the Wigner-surmise distribution (solid green line), as given by integrating Eqs. (3), are also included for reference.

gene pattern is higher than in the *self* pattern. Thus, level attraction is influenced by the different dilation patterns. (ii) However, when g^* remains constant, and the generator (n, m) is arranged in ascending order of \mathcal{D}_H (by increasing the value of $n^2 - m^2$), the peak value of $P(s)$ gradually decreases; see Fig. 3(a4).

So far, we can deduce that when an electron moves purely in these $SC(n, m, g^*)$ lattices, their LSDs tend to have a larger fraction in the small s region by increasing iteration depth g^* or Hausdorff dimension \mathcal{D}_{ge} , which suggests many fractal-shape artifacts [13,28], such as those that absorb continuous optical spectra. Since the histograms of $P(s)$ and $P(\tilde{r})$ are dependent on the different bin widths, to distinguish these $P(s)$ quantitatively, we use a stabilized integrated level-spacing distribution, $I(s) = \int_s^\infty P(t)dt$, which counts the fraction of the level spacing that is not less than s . Hence, $I(0) = 1$. This makes it simpler to grasp the level correlation behavior in the small or large s range. We integrate Eqs. (3) as a reference, and have $I_{Poi}(s) = \exp(-s)$ and $I_{GOE}(s) = \exp(-\pi s^2/4)$ for the Poisson (solid blue line) and Wigner-surmise (solid green line), respectively.

In Fig. 5, the numerical $P(s)$ for all $SC(n, m, g^*)$ lattices is shown in the form of $I(s)$. Especially, when s is larger than 3, $I(s)$ is beyond $I_{GOE}(s)$. As s decreases, $I(s)$ transitions through a region separated by $I_{GOE}(s)$ and $I_{Poi}(s)$. $I(s)$ increases faster at smaller s positions due to the degenerate and quasidegenerate levels in the studied model. When s is close to 0, $I(s)$ is below these two distributions. Additionally, the remarkable peak in $P(s) = -dI(s)/ds$ is lower than that of the histograms (four insets in Fig. 3), as a result of stripping the degenerate level behavior.

As mentioned, two distinct examples of CSs are considered. One occurs near the mobility edge where Anderson

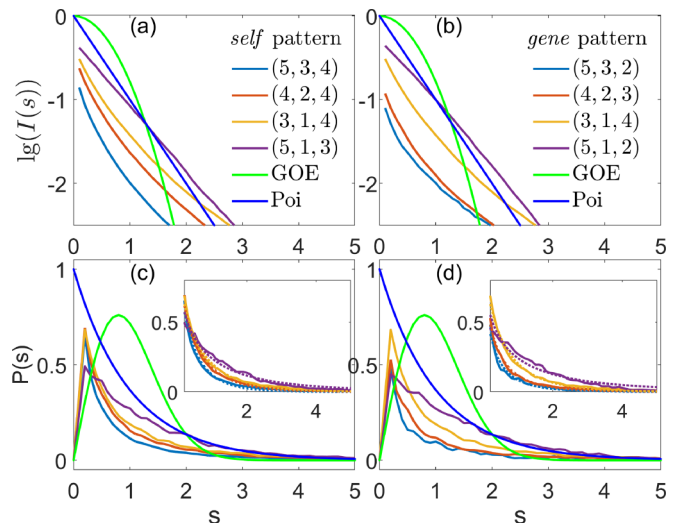


FIG. 6. The finite-size scaling of $I(s)$ and $P(s)$ is shown for two subclasses of *Sierpiński carpet* constructed using Eq. (1) with four generators listed in Table I. Under the *self* (*gene*) pattern, the lattice size Ar is 12 288 (13 824), 32 768 (32 768), 49 152 (20 736), and 65 536 (4096) from top to bottom, where the hierarchy level g is used. The linear-log scale of $I(s)$ is shown in (a) and (b), and the numerical derivative $P(s) = -dI(s)/ds$ is shown in (c) and (d). The two insets show the fitting performance of the asymptotic tail (dashed line).

transition takes place. Still using $P(s)$ terminology to extract the energy correlation in this case, its trait is between the localized and extended phases and intersects with the Poisson function $P_{Poi}(s)$ (see Fig. 1 in Ref. [82]). The value of the cross point decreases with increasing disorder strength and is less than 1.2732 (we discussed it earlier; $s = 1.2732$ is the cross point for Eqs. (3) between the two phases). The other CS is possible in *intermediate structures*. The $SC(n, m, g^*)$ lattices belong to this case, and their energy spectra are analyzed.

However, our histogram $P(s)$ differs from the crucial behavior near the mobility edge. It intersects with $P_{Poi}(s)$, which is due to the effect of degenerate levels. This can be eliminated by taking the negative derivative of $I(s)$. As seen in four insets of Fig. 3, $P(s)$ does not intersect with $P_{Poi}(s)$. The existence of $P(s)$ in a new critical phase can be attributed to the fractal lattice structure. To support this claim, a finite-size scaling analysis is performed in Fig. 6. For each generator (n, m) with the maximum computed g^* under two patterns [most $SC(n, m, g)$ lattices have a lattice size of $Ar \sim 10^4$], $P(s)$ still displays the same characteristics.

D. The Wigner-like distribution

One can observe that $P(s)$ and $I(s)$ behave on a scale as demonstrated in Figs. 3 and 5. However, the irregular fluctuations in the tail of $P(s)$ can pose some challenges when fitting it. Furthermore, the height and location of the peak of $P(s)$ can be affected by the histogram bin width when unfolding the raw levels. In Fig. 6, we use eight $SC(n, m, g^*)$ lattices to illustrate the Wigner-like behavior of $P(s)$.

The matrices in Eq. (2) are real and symmetric, and yield identical orthogonal ensembles ($\beta = 1$). This is the first indication of the linear characteristic as s approaches 0,

TABLE II. Figures 6(c) and 6(d) present the fitting parameters $(c_1, c_2, \alpha)^T$, where g holds the same value as in Figs. 6(a) and 6(b). The transcendental nature of the potential $P_{\text{fit}}(s) = c_1 s \exp(-c_2 s^\alpha)$ makes it difficult to obtain (c_1, c_2) through normalization of $P(s)$ and unitization of $\langle s \rangle$ as discussed earlier. In general, the value of α cannot be determined analytically. As an alternative, we fit $P(s) = -dI(s)/ds$ in the small s region [0,5] using a piecewise approach: the linear formula $c_1 s$ for the increasing part and the asymptotic tail $\exp(-c_2 s^\alpha)$ for the decaying part [as shown in the insets of Figs. 6(c) and 6(d)] with a 95% confidence level.

SC(n, m, g)	(5, 3)	(4, 2)	(3, 1)	(5, 1)
<i>self</i>	(3.261, 2.103, 0.818)	(3.462, 1.751, 0.797)	(3.414, 1.600, 0.768)	(2.458, 1.434, 0.584)
<i>gene</i>	(2.378, 2.471, 0.641)	(2.634, 2.146, 0.668)	(3.414, 1.600, 0.768)	(2.248, 1.426, 0.539)

as $P_{\text{GOE}}(s \rightarrow 0) \propto s$. The level clustering property becomes more pronounced as Ar increases, which results in a larger slope. Secondly, the asymptotic tail of $P(s)$ at s exceeding the value pinned by the peak of $P(s)$ but less than 1, as shown in Figs. 6(c) and 6(d), decays with an intermediate power law, as proven analytically in Ref. [55]. A shape-preserving formula $P_{\text{fit}}(s) = c_1 s \exp(-c_2 s^\alpha)$ can be used to fit these $P(s)$, but this is challenging because of the shaky tails when the data $P(s \geq 5)$ are included. Instead, we use two piecewise functions to fit three parameters (α, c_1, c_2), as listed in Table II. The performance of the fitting is demonstrated in the insets of Figs. 6(c) and 6(d).

III. DISCUSSION AND CONCLUSION

This paper investigates a noninteracting electronic gas on two SC(n, m, g^*) class lattices in 2D. We model it with a tight-binding Hamiltonian, and we obtain the energy spectra by diagonalizing the model. The study analyzes the impact of the generator(n, m), the dilation pattern, and the geometric hierarchy level g^* on the level density. The *generator* determines the local configuration of the Hamiltonian, the dilation pattern modulates the energy spectra, and g^* intensifies both mechanics and leads to level attraction with increasing its value.

Additionally, the trend of energy bandwidth changes with the three parameters is discussed. The singularly continuous energy spectra suggest a critical phase, and the energy correlation is investigated using $P(s)$ and $P(\tilde{r})$. These distributions exhibit unique behavior that corresponds to either the Poisson distribution of the localized phase or the Wigner distribution of the extended phase. The fitting function $P_{\text{fit}}(s)$ with the values of β and α is expanded using a Taylor series at the peak position, resulting in a power-law behavior.

One important point to emphasize is that despite the enumeration of several SC(n, m, g^*) lattices in Table I, the above argument still holds for more cases with larger g^* . The critical phase cannot be transitioned to other phases, such as the extended or localized phase, even by tuning the *generator*(n, m) in the SC(n, m, g^*) lattices. It should be noted that M_{ge} is always determined by the *generator*(n, m). In some extreme cases where n is significantly larger than m in the *gene* pattern,

the dilated lattice roughly approximates a 2D periodic lattice with some point or small-cluster defects, leading to some extended traits in its energy spectra, as seen in the SC(5, 1, 3) lattices.

The ramification order of *Sierpiński gasket* and the SC(n, m, g^*) lattices are finite and infinite, respectively, which causes localized patterns in the former as demonstrated in Ref. [46]. Since the *Sierpiński carpet* resembles a square periodic lattice, it is the focus of this paper. It is also recommended to investigate the SC(n, m, g^*) lattices by introducing extra topological characters such as connectivity [1,36] and lacunarity [37–41].

We would like to compare our results with several quasicrystalline examples. The critical phase is demonstrated by the multifractal spectra in a 1D *Fibonacci chain*, as reviewed in [92]. However, the situation is more complex for various *Penrose tilings* in 2D. These lattices are obtained by projecting high-dimensional cubic lattices into a lower dimension. The presence of many confined states has been revealed in some studies [93] due to the local connectivity, and the small-scale string states can be affected by the overall configuration. Macé *et al.* showed the critical state in two tilings with the SKK form [94]. The diversity of these results is largely determined by the strategies used, such as selecting the local vertex configuration, applying orientational multifold symmetry, and setting various hopping strengths between vertices [95]. In contrast, we regularly wipe out many sites (as seen in the empty site cluster in Fig. 1) in 2D rigid lattices, resulting in a normative local site configuration with a few shapes, and an open boundary in the SC(n, m, g^*) lattices. The critical states in our case can be explained by the two mechanics of aperiodicity and scaling symmetry based on g^* .

In conclusion, we modeled the system using a tight-binding model for a noninteracting electron gas confined in two SC(n, m, g^*) lattice classes percolated separately by the *self* and *gene* patterns. We analyzed the singularly continuous trait in the electronic energy spectra. Using numerical $P(s)$ and $P(\tilde{r})$ histograms, we confirmed that electronic states are embedded in a critical phase. We also fitted the Wigner-like distribution of $P(s)$ and found that it has a linear law in the small s limit and a power law in the large s limit or at the right side of the peak. These fractals have a broken translation symmetry and the long-range order of scaling symmetry, which leads to the critical phase. This differs from the well-known extended and localized phases, as well as the near mobility edge when Anderson transition occurs. A rise in the g^* value shows that the scaling symmetry is the cause of the level clustering in these lattices.

We also note that the renormalization-group approach has been used in 1D Fibonacci chains, 2D lattices such as Vicsek [8] and other fractals [56,96], and Penrose tiling [97]. However, the decimating procedures in the SC(n, m, g^*) lattices become very tedious due to their huge lattice size. For these critical states, multifractal analysis [65] is preferred. The SC(n, m, g^*) fractal topology was investigated using a straightforward hopping model, but it can be easily generalized to the Anderson model [68] and its variations [98–100], or to include two-body interactions [91]. Alternatively, other particles such as phonons are found in quasicrystals [101] and fractals.

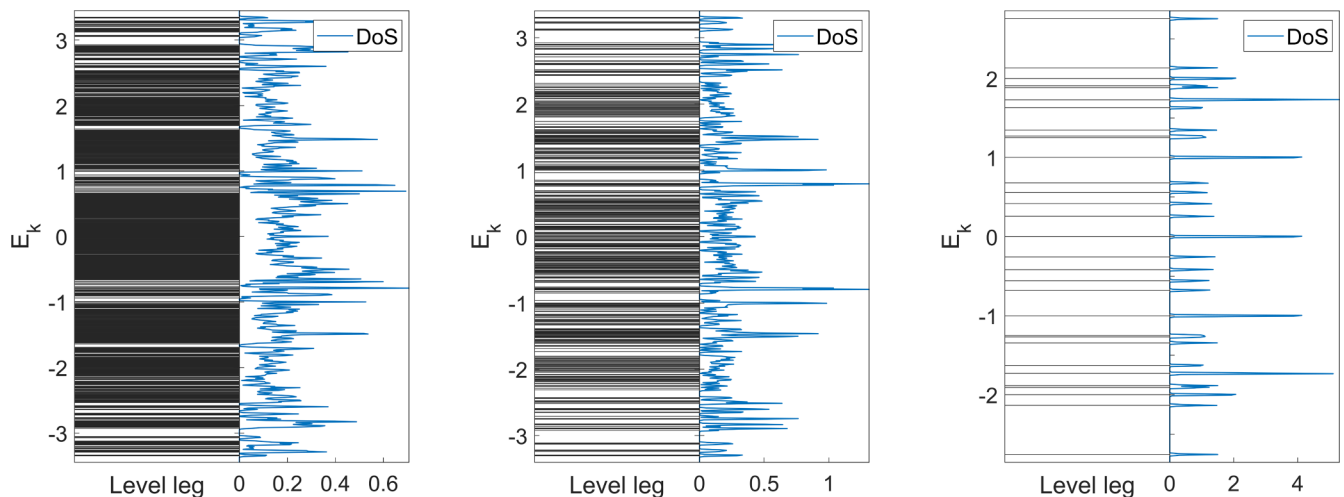


FIG. 7. Level legs and DOS for the tight-binding model are shown for the corresponding fractal SC(4, 2, 2) lattices produced under three patterns, from left to right: the *self*, the *gene*, and the variant of the *self* pattern (also known as the *vari* pattern).

ACKNOWLEDGMENTS

We are grateful for the comments from Achille Mauri and Tjacco Koskamp on this project. This work was supported by the National Natural Science Foundation of China (Grant No. 12174291) and the National Key R&D Program of China (Grant No. 2018YFA0305800), and Natural Science Foundation of Hubei Province, China (2020CFA041), and computational resources from the Supercomputing Center of Wuhan University. Q.Y. acknowledges the grant support by the China Scholarship Council (CSC) through file No. 202006270212 when attending Radboud University in the Netherlands. X.Y. is supported by China Scholarship Council (CSC) under Grant No. 202106270050.

We provide additional analysis in two Appendixes: (i) the discrete level distributions and their regularized density of state are presented, and (ii) the numerical unfolding technique for the raw level sequences $E_1 \leq E_2 < \dots < E_k \dots, k = 3, 4, \dots, \text{Dim}(H)$ is described. These new levels are then used for the $P(s)$ statistics.

APPENDIX A: THE LEVEL-DISTRIBUTION DENSITY

We present a study of single electron hopping in three SC(n, m, g^*) lattices using the tight-binding model. The lattices are constructed under three patterns: the *self*, *gene*, and *vari* patterns, with the latter being a variation of the *self* pattern. The levels are obtained from direct diagonalization of the Hamiltonian and are shown in terms of the level leg and density of state (DOS). To avoid needlelike peaks in the DOS, the Dirac function is blurred by using either a Gaussian or Lorentz function [65,102] with a small energy window of 0.005.

We compare the three pattern-based lattices by setting the same geometrical hierarchy g^* , where a smaller g^* results in more obvious nearby local clusters. In this study, we put $g^* = 2$. In Fig. 7, we highlight the prominent symmetry about $E = 0$. In the *vari* pattern, some separate vertex subclusters in the SC(n, m, g^*) lattice result in subblocks in the Hilbert space,

manifesting as typical but small clusters in the energy spectra. Increasing g^* can increase the peak value but does not alter the locations where the peaks are pinned (as seen in the right panel of Fig. 7).

In contrast, the DOSs in the *self* and *gene* patterns are coherent and dense, as shown in the left and middle panels of Fig. 7. This is due to the lack of discrete vortex subclusters in their lattices. Both patterns display a uniform trend, which can be adjusted through the choice of pattern and the increase of g^* . In the main text, we have discussed the impact of the generator(n, m) and g^* on the lattices. There are some differences between the two patterns. The *gene* pattern exhibits stronger level attraction near the band center, while the *self* pattern has blocky spectra. It is worth noting that the *self* pattern with $g^* = 2$ has more vertexes, thus it appears to have more level legs.

APPENDIX B: THE UNFOLDING PROCEDURES FOR THE LEVEL-SPACING STATISTICS

The unfolding procedure aims to eliminate the discontinuity of the integrated density of states (IDOS) by using a cubic spline and to obtain a monotonous function $\eta(E)$; see the two curves of Fig. 8(b). The IDOS is defined as $\text{IDOS}(E) = 1/Ar \sum_m \Theta(E - E_m)$, where $\Theta(t)$ is a cumulative count function for $t \leq 0$. Less than 5% of numerical points violate the monotonicity of $\text{IDOS}(E)$, and these points are skipped to ensure the monotonicity of $\eta(E)$.

The derivative of $\eta(E)$, $\rho(E) = d\eta(E)/dE$, is confirmed to be correct using two different methods. One method is by comparing $\rho(E)$ to a histogram-like DOS in Fig. 8(c1). The results show that both are primarily the same, with the horizontal offset caused by the forward Euler method. The other method is by comparing $\rho(E)$ to a smoothlike DOS in Fig. 8(c2), which is obtained using a Gaussian or Lorentz blurring function. The regularized DOS $\rho_\sigma(E)$ with these two functions serves as an envelope of the numerical derivative $\rho(E)$.

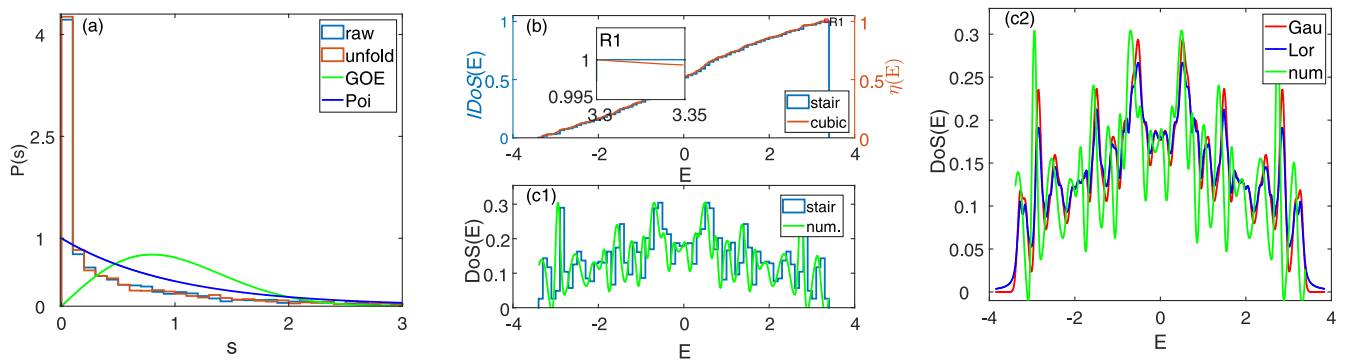


FIG. 8. $P(s)$ after and before the unfolding procedure, the level spacing, and the DOS for the tight-binding model on the fractal SC(4, 2, 2) lattice produced under three patterns are shown in (a). For comparison, the histograms of $P_{\text{GOE}}(s)$ and $P_{\text{Poi}}(s)$ are added. $P(s)$ is derived indirectly from the cubic interpolation function $\eta(E)$, which is obtained from the integral DOS (IDOS) in (b). In some regions, the monotonicity of $\eta(E)$ is violated (an inset shows the zoomed-out red rectangle R1). In (c1), the derivative of $\eta(E)$ (solid green) is compared with the original histogram (stair blue) as the DOS. In (c2), the Gaussian (solid red) or Lorentz (solid blue) function $\rho_\sigma(E)$ regularizes the needlelike energy spectra $\rho(E) = \sum_n \delta(E - E_n)$, where $\sigma = 0.05$ is a small energy window. Both are compared with $\rho(E) = d\eta(E)/dE$ (solid green).

To obtain the new level spacings ε_i for $P(s)$, the raw levels E_i are interpolated using $\varepsilon_i = \eta(E_i)$. Figure 8(a) shows $P(s)$

using an illustrated SC(4, 2, 2) lattice, with both the basic and new level sequences shown.

- [1] B. B. Mandelbrot, *The Fractal Geometry of Nature* (W. H. Freeman and Company, New York, 1991), Vol. 1.
- [2] M. Schroeder, *Fractals, Chaos, Power Laws: Minutes from an Infinite Paradise* (W. H. Freeman and Company, New York, 2009).
- [3] K. Falconer, *Fractal Geometry: Mathematical Foundations and Applications* (Wiley, Chichester, 2004).
- [4] T. Nakayama and K. Yakubo, *Fractal Concepts in Condensed Matter Physics* (Springer Science & Business Media, New York, 2003), Vol. 140.
- [5] B. Mandelbrot, *Fractals* (Freeman, San Francisco, 1977).
- [6] W. Sierpinski, Sur une courbe dont tout point est un point de ramification, *C. R. Acad. Sci.* **160**, 302 (1915).
- [7] T. Vicsek, Fractal models for diffusion controlled aggregation, *J. Phys. A* **16**, L647 (1983).
- [8] J. Q. You, C.-H. Lam, F. Nori, and L. M. Sander, Exact renormalization-group approach to the generating function of the vicsek fractal, *Phys. Rev. E* **48**, R4183(R) (1993).
- [9] H. Koch, Une méthode géométrique élémentaire pour l'étude de certaines questions de la théorie des courbes planes, *Acta Math.* **30**, 145 (1906).
- [10] C. Even, S. Russ, V. Repain, P. Pieranski, and B. Sapoval, Localizations in Fractal Drums: An Experimental Study, *Phys. Rev. Lett.* **83**, 726 (1999).
- [11] P.-z. Wong and Q.-z. Cao, Correlation function and structure factor for a mass fractal bounded by a surface fractal, *Phys. Rev. B* **45**, 7627 (1992).
- [12] B. Sapoval and T. Gobron, Vibrations of strongly irregular or fractal resonators, *Phys. Rev. E* **47**, 3013 (1993).
- [13] R. Kopelman, M. Shortreed, Z.-Y. Shi, W. Tan, Z. Xu, J. S. Moore, A. Bar-Haim, and J. Klafter, Spectroscopic Evidence for Excitonic Localization in Fractal Antenna Supermolecules, *Phys. Rev. Lett.* **78**, 1239 (1997).
- [14] F. L. Metz and I. Neri, Localization and Universality of Eigenvectors in Directed Random Graphs, *Phys. Rev. Lett.* **126**, 040604 (2021).
- [15] Y. Matsuki, K. Ikeda, and M. Koshino, Fractal defect states in the hofstadter butterfly, *Phys. Rev. B* **104**, 035305 (2021).
- [16] J. Q. You and Q. B. Yang, Dynamical maps and cantor-like spectra for a class of one-dimensional quasiperiodic lattices, *J. Phys.: Condens. Matter* **2**, 2093 (1990).
- [17] T. G. Pedersen, Graphene fractals: Energy gap and spin polarization, *Phys. Rev. B* **101**, 235427 (2020).
- [18] D. Wójcik, I. Białynicki-Birula, and K. Życzkowski, Time Evolution of Quantum Fractals, *Phys. Rev. Lett.* **85**, 5022 (2000).
- [19] R. Rammal, Nature of eigenstates on fractal structures, *Phys. Rev. B* **28**, 4871 (1983).
- [20] W. A. Schwalm and M. K. Schwalm, Electronic properties of fractal-glass models, *Phys. Rev. B* **39**, 12872 (1989).
- [21] W. A. Schwalm and M. K. Schwalm, Explicit orbits for renormalization maps for green functions on fractal lattices, *Phys. Rev. B* **47**, 7847 (1993).
- [22] R. Penrose, The role of aesthetics in pure and applied mathematical research, *Bull. Inst. Math. Appl.* **10**, 266 (1974).
- [23] M. Gardner, Mathematical games, *Sci. Am.* **237**, 120 (1977).
- [24] D. Shechtman, I. Blech, D. Gratias, and J. W. Cahn, Metallic Phase with Long-Range Orientational Order and no Translational Symmetry, *Phys. Rev. Lett.* **53**, 1951 (1984).
- [25] D. Levine and P. J. Steinhardt, Quasicrystals: A New Class of Ordered Structures, *Phys. Rev. Lett.* **53**, 2477 (1984).
- [26] G. R. Newkome, P. Wang, C. N. Moorefield, T. J. Cho, P. P. Mohapatra, S. Li, S.-H. Hwang, O. Lukoyanova, L. Echegoyen, J. A. Palagallo, V. Iancu, and S.-W. Hla, Nanoassembly of a fractal polymer: A molecular "sierpinski hexagonal gasket," *Science* **312**, 1782 (2006).

- [27] J. A. Fan, W.-H. Yeo, Y. Su, Y. Hattori, W. Lee, S.-Y. Jung, Y. Zhang, Z. Liu, H. Cheng, L. Falgout, M. Bajema, T. Coleman, D. Gregoire, R. J. Larsen, Y. Huang, and J. A. Rogers, Fractal design concepts for stretchable electronics, *Nat. Commun.* **5**, 3266 (2014).
- [28] A. Hernando, M. Sulc, and J. Vanicek, Spectral properties of electrons in fractal nanowires (2015).
- [29] J. Shang, Y. Wang, M. Chen, J. Dai, X. Zhou, J. Kuttner, G. Hilt, X. Shao, J. M. Gottfried, and K. Wu, Assembling molecular sierpiński triangle fractals, *Nat. Chem.* **7**, 389 (2015).
- [30] X. Zhang, N. Li, L. Liu, G. Gu, C. Li, H. Tang, L. Peng, S. Hou, and Y. Wang, Robust sierpiński triangle fractals on symmetry-mismatched $ag(100)$, *Chem. Commun.* **52**, 10578 (2016).
- [31] S. N. Kempkes, M. R. Slot, S. E. Freeney, S. J. M. Zevenhuizen, D. Vanmaekelbergh, I. Swart, and C. M. Smith, Design and characterization of electrons in a fractal geometry, *Nat. Phys.* **15**, 127 (2019).
- [32] C. Liu, Y. Zhou, G. Wang, Y. Yin, C. Li, H. Huang, D. Guan, Y. Li, S. Wang, H. Zheng, C. Liu, Y. Han, J. W. Evans, F. Liu, and J. Jia, Sierpiński Structure and Electronic Topology in Bi Thin Films on InSb(111)B Surfaces, *Phys. Rev. Lett.* **126**, 176102 (2021).
- [33] Y. Gefen, B. B. Mandelbrot, and A. Aharony, Critical Phenomena on Fractal Lattices, *Phys. Rev. Lett.* **45**, 855 (1980).
- [34] S. Ohta and H. Honjo, Growth Probability Distribution in Irregular Fractal-Like Crystal Growth of Ammonium Chloride, *Phys. Rev. Lett.* **60**, 611 (1988).
- [35] Y. Bo-Ming and Y. Kai-Lun, Numerical evidence of the critical percolation probability $p_c = 1$ for site problems on sierpinski gaskets, *J. Phys. A* **21**, 3269 (1988).
- [36] M. Suzuki, Phase Transition and Fractals, *Prog. Theor. Phys.* **69**, 65 (1983).
- [37] Y. Gefen, Y. Meir, B. B. Mandelbrot, and A. Aharony, Geometric Implementation of Hypercubic Lattices with Non-integer Dimensionality by Use of Low Lacunarity Fractal Lattices, *Phys. Rev. Lett.* **50**, 145 (1983).
- [38] B. Lin and Z. R. Yang, A suggested lacunarity expression for sierpinski carpets, *J. Phys. A* **19**, L49 (1986).
- [39] Y. Taguchi, Lacunarity and universality, *J. Phys. A* **20**, 6611 (1987).
- [40] B. Lin, Classification and universal properties of sierpinski carpets, *J. Phys. A* **20**, L163 (1987).
- [41] Y.-K. Wu, Lacunarity and universality, *J. Phys. A* **21**, 4251 (1988).
- [42] E. van Veen, S. Yuan, M. I. Katsnelson, M. Polini, and A. Tomadin, Quantum transport in sierpinski carpets, *Phys. Rev. B* **93**, 115428 (2016).
- [43] X.-Y. Xu, X.-W. Wang, D.-Y. Chen, C. M. Smith, and X.-M. Jin, Quantum transport in fractal networks, *Nat. Photon.* **15**, 703 (2021).
- [44] A. A. Iliasov, M. I. Katsnelson, and S. Yuan, Hall conductivity of a sierpiński carpet, *Phys. Rev. B* **101**, 045413 (2020).
- [45] E. van Veen, A. Tomadin, M. Polini, M. I. Katsnelson, and S. Yuan, Optical conductivity of a quantum electron gas in a sierpinski carpet, *Phys. Rev. B* **96**, 235438 (2017).
- [46] T. Westerhout, E. van Veen, M. I. Katsnelson, and S. Yuan, Plasmon confinement in fractal quantum systems, *Phys. Rev. B* **97**, 205434 (2018).
- [47] Y. Gefen, A. Aharony, and B. B. Mandelbrot, Phase transitions on fractals. III. infinitely ramified lattices, *J. Phys. A* **17**, 1277 (1984).
- [48] E. Akkermans, G. V. Dunne, and A. Teplyaev, Thermodynamics of Photons on Fractals, *Phys. Rev. Lett.* **105**, 230407 (2010).
- [49] R. Rammal, Spectrum of harmonic excitations on fractals, *J. Phys. France* **45**, 191 (1984).
- [50] B. Pal, P. Patra, J. P. Saha, and A. Chakrabarti, Engineering wave localization in a fractal waveguide network, *Phys. Rev. A* **87**, 023814 (2013).
- [51] X. Xia, K. Huang, S. Wang, and X. Li, Exact mobility edges in the non-hermitian t_1-t_2 model: Theory and possible experimental realizations, *Phys. Rev. B* **105**, 014207 (2022).
- [52] X. Yang, W. Zhou, P. Zhao, and S. Yuan, Confined electrons in effective plane fractals, *Phys. Rev. B* **102**, 245425 (2020).
- [53] A. S. Balankin, The topological hausdorff dimension and transport properties of sierpiński carpets, *Phys. Lett. A* **381**, 2801 (2017).
- [54] J. Feder, *Fractals* (Springer Science & Business Media, New York, 2013).
- [55] A. A. Iliasov, M. I. Katsnelson, and S. Yuan, Power-law energy level spacing distributions in fractals, *Phys. Rev. B* **99**, 075402 (2019).
- [56] A. A. Iliasov, M. I. Katsnelson, and S. Yuan, Linearized spectral decimation in fractals, *Phys. Rev. B* **102**, 075440 (2020).
- [57] F. J. Dyson, Statistical theory of the energy levels of complex systems. I, *J. Math. Phys.* **3**, 140 (1962).
- [58] F. J. Dyson, Statistical theory of the energy levels of complex systems. II, *J. Math. Phys.* **3**, 157 (1962).
- [59] F. J. Dyson, Statistical theory of the energy levels of complex systems. III, *J. Math. Phys.* **3**, 166 (1962).
- [60] J. X. Zhong, U. Grimm, R. A. Römer, and M. Schreiber, Level-Spacing Distributions of Planar Quasiperiodic Tight-Binding Models, *Phys. Rev. Lett.* **80**, 3996 (1998).
- [61] G. Akemann, J. Baik, and P. Di Francesco, *The Oxford Handbook of Random Matrix Theory* (Oxford University Press, Oxford, 2015).
- [62] Q. Yao, M. I. Katsnelson, and S. Yuan, For $SC(n, m, g^*)$ lattice, one-parameter scaling at metal-insulator transition can be explored in the fractal dimension (unpublished).
- [63] Here we can estimate that when g increases by a unit, the value $N = \text{Dim}(H)$ extends eight times for the *self* pattern of $\mathcal{N} = 8$, however for the *gene* pattern, it is larger and depends on the special choice of the generator (n, m) , up to $n^2 - m^2$ times. It brings the unaffordable computational overhead at time $o(N^3)$ and at memory $o(N^2)$.
- [64] For a quasidegenerate (or degenerate) level cluster, their states trend to nonorthogonal between each other, and the spatial overlapping in a fractal lattice causes the correlation between these levels. Using the participation ratio or generalized multi-fractal analysis, we further clarify the diversity between these critical states.
- [65] Q. Yao, X.-T. Yang, A. A. Iliasov, M. I. Katsnelson, and S. Yuan, In a planar Sierpiński fractal lattice, wave functions in critical phase can be found and analyzed by multi-fractality and sub-diffusion behavior (unpublished).
- [66] K. Machida and M. Fujita, Quantum energy spectra and one-dimensional quasiperiodic systems, *Phys. Rev. B* **34**, 7367 (1986).

- [67] F. Bloch, On the quantum mechanics of electrons in crystal lattices, *Mag. Phys.* **52**, 555 (1929).
- [68] P. W. Anderson, Absence of diffusion in certain random lattices, *Phys. Rev.* **109**, 1492 (1958).
- [69] J. S. Howland, Perturbation theory of dense point spectra, *J. Funct. Anal.* **74**, 52 (1987).
- [70] H. Hiramoto and M. Kohmoto, New Localization in a Quasiperiodic System, *Phys. Rev. Lett.* **62**, 2714 (1989).
- [71] T. Fujiwara, M. Kohmoto, and T. Tokihiro, Multifractal wave functions on a fibonacci lattice, *Phys. Rev. B* **40**, 7413 (1989).
- [72] H. Hiramoto and M. Kohmoto, Electronic spectral and wavefunction properties of one-dimensional quasiperiodic systems: a scaling approach, *Int. J. Mod. Phys. B* **06**, 281 (1992).
- [73] J. Vidal, R. Mosseri, and B. Douçot, Aharonov-Bohm Cages in Two-Dimensional Structures, *Phys. Rev. Lett.* **81**, 5888 (1998).
- [74] J. Vidal, P. Butaud, B. Douçot, and R. Mosseri, Disorder and interactions in aharonov-bohm cages, *Phys. Rev. B* **64**, 155306 (2001).
- [75] S. Mukherjee, M. Di Liberto, P. Öhberg, R. R. Thomson, and N. Goldman, Experimental Observation of Aharonov-Bohm Cages in Photonic Lattices, *Phys. Rev. Lett.* **121**, 075502 (2018).
- [76] O. Lesser and R. Lifshitz, Emergence of quasiperiodic bloch wave functions in quasicrystals, *Phys. Rev. Res.* **4**, 013226 (2022).
- [77] F. J. Dyson and M. L. Mehta, Statistical theory of the energy levels of complex systems. IV, *J. Math. Phys.* **4**, 701 (1963).
- [78] T. Guhr, A. Müller-Groeling, and H. A. Weidenmüller, Random-matrix theories in quantum physics: common concepts, *Phys. Rep.* **299**, 189 (1998).
- [79] T. A. Brody, J. Flores, J. B. French, P. A. Mello, A. Pandey, and S. S. M. Wong, Random-matrix physics: spectrum and strength fluctuations, *Rev. Mod. Phys.* **53**, 385 (1981).
- [80] E. J. Torres-Herrera, J. A. Méndez-Bermúdez, and L. F. Santos, Level repulsion and dynamics in the finite one-dimensional anderson model, *Phys. Rev. E* **100**, 022142 (2019).
- [81] J. M. G. Gómez, R. A. Molina, A. Relaño, and J. Retamosa, Misleading signatures of quantum chaos, *Phys. Rev. E* **66**, 036209 (2002).
- [82] I. K. Zharekshv and B. Kramer, Scaling of level statistics at the disorder-induced metal-insulator transition, *Phys. Rev. B* **51**, 17239 (1995).
- [83] V. Oganessian and D. A. Huse, Localization of interacting fermions at high temperature, *Phys. Rev. B* **75**, 155111 (2007).
- [84] O. Giraud, N. Macé, E. Vernier, and F. Alet, Probing Symmetries of Quantum Many-Body Systems through Gap Ratio Statistics, *Phys. Rev. X* **12**, 011006 (2022).
- [85] L. Sá, P. Ribeiro, and T. Prosen, Complex Spacing Ratios: A Signature of Dissipative Quantum Chaos, *Phys. Rev. X* **10**, 021019 (2020).
- [86] T. A. Brody, A statistical measure for the repulsion of energy levels, *Lett. Nuovo Cimento* **7**, 482 (1973).
- [87] G. Casati, F. Izrailev, and L. Molinari, Scaling properties of the eigenvalue spacing distribution for band random matrices, *J. Phys. A* **24**, 4755 (1991).
- [88] A. Aronov, V. Kravtsov, and I. Lerner, The Level Spacing Distribution Near the Anderson Transition, *Pis'ma Zh. Eksp. Teor. Fiz.* **59**, 40 (1994) [*JETP Lett.* **59**, 39 (1994)].
- [89] I. Varga, E. Hofstetter, M. Schreiber, and J. Pipek, Shape analysis of the level-spacing distribution around the metal-insulator transition in the three-dimensional anderson model, *Phys. Rev. B* **52**, 7783 (1995).
- [90] Y. Y. Atas, E. Bogomolny, O. Giraud, and G. Roux, Distribution of the Ratio of Consecutive Level Spacings in Random Matrix Ensembles, *Phys. Rev. Lett.* **110**, 084101 (2013).
- [91] J. De Marco, L. Tolle, C.-M. Halati, A. Sheikhan, A. M. Läuchli, and C. Kollath, Level statistics of the one-dimensional ionic hubbard model, *Phys. Rev. Res.* **4**, 033119 (2022).
- [92] A. Jagannathan, The fibonacci quasicrystal: Case study of hidden dimensions and multifractality, *Rev. Mod. Phys.* **93**, 045001 (2021).
- [93] M. Arai, T. Tokihiro, T. Fujiwara, and M. Kohmoto, Strictly localized states on a two-dimensional penrose lattice, *Phys. Rev. B* **38**, 1621 (1988).
- [94] N. Macé, A. Jagannathan, P. Kalugin, R. Mosseri, and F. Piéchon, Critical eigenstates and their properties in one- and two-dimensional quasicrystals, *Phys. Rev. B* **96**, 045138 (2017).
- [95] T. Odagaki and D. Nguyen, Electronic and vibrational spectra of two-dimensional quasicrystals, *Phys. Rev. B* **33**, 2184 (1986).
- [96] E. Domany, S. Alexander, D. Bensimon, and L. P. Kadanoff, Solutions to the schrödinger equation on some fractal lattices, *Phys. Rev. B* **28**, 3110 (1983).
- [97] J. Q. You, J. R. Yan, J. X. Zhong, and X. H. Yan, Local electronic properties of two-dimensional penrose tilings: A renormalization-group approach, *Phys. Rev. B* **45**, 7690 (1992).
- [98] P. G. Harper, Single band motion of conduction electrons in a uniform magnetic field, *Proc. Phys. Soc. Sect. A* **68**, 874 (1955).
- [99] S. Aubry and G. André, Analyticity breaking and anderson localization in incommensurate lattices, *Ann. Israel Phys. Soc.* **3**, 18 (1980).
- [100] P. G. Harper, The general motion of conduction electrons in a uniform magnetic field, with application to the diamagnetism of metals, *Proc. Phys. Soc. Sect. A* **68**, 879 (1955).
- [101] F. Salazar, C. Wang, A. Gelover-Santiago, A. Zentella-Dehesa, G. Naumis, and J. Talamantes, Phonon localization in quasiperiodic systems, *J. Non-Cryst. Solids* **329**, 167 (2003), 7th Int. Workshop on Non-Crystalline Solids.
- [102] L. Lin, Y. Saad, and C. Yang, Approximating spectral densities of large matrices, *SIAM Rev.* **58**, 34 (2016).